Multiphysical modeling of the photopolymerization process for additive manufacturing of ceramics

Please check the document version of this publication:

• A submitted manuscript is the version of the article upon submission and before peer-review. There can be important differences between the submitted version and the official published version of record. People interested in the research are advised to contact the author for the final version of the publication, or visit the DOI to the publisher's website.
• The final author version and the galley proof are versions of the publication after peer review.
• The final published version features the final layout of the paper including the volume, issue and page numbers.

Link to publication

Multiphysical modeling of the photopolymerization process for additive manufacturing of ceramics

S. Westbeek[a,b], J.A.W. van Dommelen[a,*], J.J.C. Remmers[a], M.G.D. Geers[a]

[a]*Eindhoven University of Technology, Department of Mechanical Engineering, P.O. Box 513, 5600 MB Eindhoven, The Netherlands*
[b]*AMSYSTEMS Center, De Rondom 1, 5612 AP Eindhoven, The Netherlands*

Abstract

Additive manufacturing (AM) of ceramics through vat photopolymerization is a promising technique in which a ceramic filled photopolymer is selectively solidified in a layerwise manner towards the final part geometry. Large scale adoption and optimization of AM for ceramics requires an in depth understanding of the process, which is pursued through a theoretical-numerical approach in this work. A modeling framework is proposed that integrates the coupled effect of four relevant physical mechanisms: *(i)* light propagation through the heterogeneous matter; *(ii)* conversion of the photopolymer; *(iii)* thermal effects and *(iv)* evolution of mechanical properties upon solidification. Interestingly, the inclusion of ceramic particles (compared to the regular vat photopolymerization process) has a marked influence for each individual physical mechanism. Even though the individual key ingredients are established, the coupled and integrated framework provides innovative insights, demonstrating how difficult it is to achieve homogeneous polymerization for ceramic-filled resins.

Keywords: additive manufacturing, ceramics, vat photopolymerization, process modeling, coupled multiphysics, micro-scale modeling

*Corresponding author
Email address:* `j.a.w.v.dommelen@tue.nl` (J.A.W. van Dommelen)

Nomenclature

α Absorption/attenuation coefficient [1/m]

γ Electric conductivity [Sm]

ΔH Polymerization heat [J/mol]

ϵ Electrical permittivity [F/m]

$\boldsymbol{\varepsilon}$ Strain tensor [-]

ζ Wave number [rad/m]

κ Extinction coefficient [-]

λ Wavelength [m]

μ Magnetic permeability [H/m]

ν Poisson's ratio [-]

ρ Volumetric mass density [kg/m^3]

$\boldsymbol{\sigma}$ Stress tensor [Pa]

υ Thermal expansion coefficient [1/K]

ϕ Particle filling fraction [-]

ψ Quantum yield for initiation [-]

ω Angular frequency [rad/s]

a Molar absorptivity [L/mol m]

c Speed of light [m/s]

c_p Heat capacity [J/(kg K)]

E Young's modulus [Pa]

$\vec{E}$ Electric field [V/m]

$\vec{H}$ Magnetic field [A/m]

I Intensity/irradiance [W/m^2]

$\vec{J}$ Electric current [V]

k Thermal conductivity [W/(m K)]

k_p Propagation rate constant [L/(mol s)]

k_t Termination rate constant [L/(mol s)]

n Refractive index [-]

p Conversion level of polymerization [-]

$\mathcal{P}_M$ Polymerization constant [m/$\sqrt{\text{W}}$]

$\vec{S}$ Poynting vector [W/m^2]

t Time [s]

T Temperature [K]

V Volume [m^3]

$[x]$ Concentration of species x [mol/l]

1. Introduction

The speed at which rapid prototyping evolved to additive manufacturing (AM), or 3D printing, illustrates how strongly its potential evolved in the past decade[1]. Many different AM technologies exist to fabricate ceramics [2]. The different techniques can be classified into seven distinct categories according to ASTM/ISO standardization [1]. The majority of the research has, however, focused on the development of porous structures. A twofold justification can be recognized for this [3]. On the one hand, the most logical motivation is that AM distinguishes itself from conventional production techniques by enabling of complex shapes with controllable porosity. On the other hand many of the available techniques are intrinsically suited for targeted shapes and detailed structures. For the particular additive manufacturing technique considered here, i.e. a patterned photopolymerization of individual layers (termed vat photopolymerization or stereolithography), these trends can also be recognized [4].

In order to produce ceramic parts through vat photopolymerization, additional processing steps are introduced, as illustrated in Fig. 1. Initially, ceramic powder is mixed
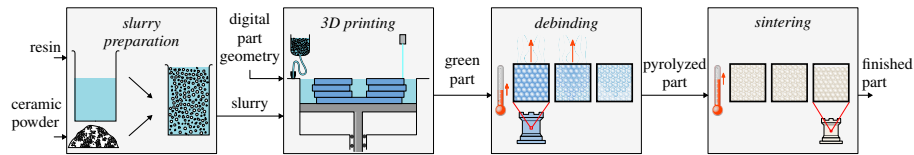
Figure 1: Overview of the ceramic additive manufacturing process by vat photopolymerization.

into the photopolymeric solution to a high filling degree such that a viscous suspension, a slurry, is obtained. Based on a three-dimensional computer model of the desired geometry, the subsequent vat photopolymerization is a repetitive process of depositing a layer of slurry, selective illumination by UV light and lowering the building platform [5]. This AM technique ultimately results in the so-called green part, which can be considered as an intermediate composite part of ceramic inclusions in a polymer matrix. To retrieve the final dense ceramic, a subsequent pyrolysis and sintering step are required at different elevated temperatures, respectively to evaporate the polymer binder and sinter the dense monolithic part.

3

The addition of ceramic inclusions has a profound effect on the relevant physical processes in the stereolithography step. Starting already with the layer deposition, i.e. recoating, the higher viscosity needs to be considered since it increases the shear forces [3]. Upon illumination, the inclusions introduce significant light scattering, which is dominated by the difference in refractive index between the resin and the ceramic [4, 6–9]. As shown experimentally, the resulting cured polymer geometry can be considerably different from the expected geometry for unfilled liquids (as a function of the light source). Furthermore, the addition of solid particles reduces effective shrinkage, counter-acted by the polymerization shrinkage, which leads to increased stress concentrations.

Generally, the limiting factors in the wide adoption of AM in industry are reproducibility, productivity and scalability [10]. For ceramics in specific, the main challenges are: increasing the monolithic part density, increasing feasible product sizes and wall thickness and avoiding the formation of cracks [3]. A better understanding of the ceramics stereolithography process, in this case pursued through numerical modeling, is considered key in overcoming these problems [10].

Such a modeling approach should include the physical processes mentioned above. Different authors have used numerical modeling to improve the understanding of the stereolithography process, starting from Jacobs' cure depth model [5]. In subsequent works, a distinction can be made between attempts to capture the effect of the layered nature of the AM process [11–14] or to incorporate more detailed physics affecting the polymerized profile as a function of the illumination source [15–19]. Whereas the first category of approaches is applicable for AM in general, the latter type of models is very specific for a certain AM technique. In comparison, for the modeling of laser powder bed or direct deposition processes the laser-material interaction induces sintering or melting directly by an increased temperature [20, 21].

The model presented in this paper can be classified among the latter category, but, to the authors' knowledge, distinguishes itself in developing a framework that relates light penetration via conversion to the buildup of mechanical properties, with full account for the presence of the inclusions. At the same time, the effect of secondary physical phenomena such as generation of heat, chemical/thermal strain and the development of

4

internal stresses can be accounted for. The theoretical formulation of this framework will be addressed first, after which dedicated verification steps of the implementation are conducted. The relevance of the developed model will be demonstrated using an academic example problem.

2. Physical and mathematical framework

The photopolymerization process of the filled resin is a complex multiphysical process. This section addresses the relevant physical ingredients of the modeling approach, followed by a description of the proposed multiphysical coupling.

2.1. Illumination

The first relevant phenomenon is the light scattering introduced upon illumination/ irradiation of the slurry. Before addressing the particulate medium, the conventional vat photopolymerization modeling process for homogeneous media is reviewed.

Absorption. In a homogeneous medium without the presence of scatterers, the attenuation of light is typically absorption dominated [22]. In that specific case, the absorbance A is formulated through the Beer-Lambert law as [23]

$$A = -\log\left(\frac{I}{I_0}\right) = a[C^*]l, \tag{1}$$

where I_0 and I are the incident intensity and the intensity at depth l into the sample, respectively, a is the molar absorptivity and $[C^*]$ the concentration of the absorbing species. A relation providing the irradiance at a particular depth in the sample is obtained by rewriting Eq. (1) as [24, 25]

$$I(l) = I_0 e^{-\ln(10)a[C^*]l} = I_0 e^{-\alpha l} \quad \left[\text{W/m}^2\right], \tag{2}$$

in which $\alpha = \ln(10)a[C^*]$ denotes the absorption/attenuation coefficient.

Within the field of vat photopolymerization, a modified version of Eq. (2) is often applied, which uses the so-called penetration depth D_p [5] as

$$D_p = \frac{1}{\ln(10)a[C^*]}. \tag{3}$$

5

Substituting the latter into Eq. (2) gives

$$I(l) = I_0 e^{-l/D_p}, \tag{4}$$

from which D_p can be interpreted as the depth where the irradiance has reduced to about 37 % (cf. $e^{-1} = 0.3679$) of the initial value [1, 5].

Wavelike behavior. The impact of the inclusions on the vat photopolymerization process of ceramic filled resins has been clearly illustrated by e.g. Refs. [4, 6–9]. Experimental investigation shows that the ratio of cure depth to cure width decreases both for increasing the illumination intensity and for an increase in refractive index difference between the resin and the inclusions [4].

As already stated before, the Beer-Lambert law is no longer adequate if scattering is to be accounted for. Different theoretical and numerical methods exist to incorporate the effect of the ceramic inclusions. Due to the large filling fraction and the small difference between light wavelength and particle dimensions, both in the order of 1 μm, a wave description is required here [26, 27]. Phenomena such as interference and diffraction play an important role in this regime, where the ratio of the feature size to wavelength is smaller than ten. Refractive optics such as ray tracing are not able to capture these phenomena and should be applied only when the scattering object is over 100 times the size of the wavelength [26]. Additionally, the large filling fraction introduces so-called multiple scattering which prohibits the application of single-scattering approaches such as the theoretical Mie theory, which is only applicable for highly dilute suspensions [27, 28]. Within this paper, the wave response is predicted solving Maxwell's equations for electromagnetics using the finite element method (FEM) [29, 30].

In a finite element framework, the Maxwell equations (which are a function of both the magnetic and electric fields) are usually rewritten into a single formula. Constitutive relations are used to eliminate the dependence of the electric field on the magnetic field or vice versa [31–33]. In the former case, the equilibrium equation can be written as [34]

$$\vec{\nabla} \times \left(\frac{1}{\mu} \vec{\nabla} \times \vec{E} \right) + \epsilon \frac{\partial^2 \vec{E}}{\partial t^2} + \gamma \frac{\partial \vec{E}}{\partial t} = -\frac{\partial \vec{J}^{\text{imp}}}{\partial t}, \tag{5}$$

where $\vec{E}$ is the electric field, μ the magnetic permeability, ϵ the electrical permittivity, γ the electric conductivity, $\vec{\nabla} \times$ the curl-operator and $\vec{J}^{\text{imp}}$ the imposed electrical current

density and t denotes the time. By definition the total current density $\vec{J}$ is equal to $\vec{J}^{\mathrm{imp}} + \gamma \vec{E}$. When written in the frequency domain, under the assumption that the electric field takes the form $\vec{E}\left(\vec{x}, t\right) = \Re\left(\vec{E}(\vec{x})e^{i\omega t}\right)$ [34, 35], the relation yields

$$\vec{\nabla} \times \left(\frac{1}{\mu}\vec{\nabla} \times \vec{E}\right) - \left(\omega^2 \epsilon - i\omega\gamma\right)\vec{E} = -i\omega\vec{J}^{\mathrm{imp}}, \tag{6}$$

where ω is the angular frequency. The imposed current density will be assumed zero in the following. Furthermore, a separation of the material properties, i.e. μ, ϵ and γ into $\mu_0\mu_r$, $\epsilon_0\epsilon_r$ and $\gamma_0\gamma_r$, is introduced, where the property x, i.e. either μ, ϵ or γ, can be divided into a contribution in free space x_0 with appropriate units and a relative one x_r. Additionally, the light wave number ζ in free space is introduced as [35, 36]

$$\zeta_0 = \frac{\omega}{c_0} = \omega\sqrt{\mu_0\epsilon_0} \tag{7}$$

with c_0 the speed of light in vacuum. This allows rewriting Eq. (6) as

$$\vec{\nabla} \times \left(\frac{1}{\mu_r}\vec{\nabla} \times \vec{E}\right) - \zeta_0^2\left(\epsilon_r - \frac{i\gamma}{\epsilon_0\omega}\right)\vec{E} = \vec{0}. \tag{8}$$

The latter is often simplified further using a complex form of the permittivity, e.g.

$$\tilde{\epsilon}_r = \epsilon_r - \frac{i\gamma}{\epsilon_0\omega}. \tag{9}$$

Since ceramics and polymers are typically dielectric, the relative magnetic permeability μ_r is (very close to) unity [36]. Consequently, the complex relative permittivity can be written as

$$\tilde{\epsilon}_r = (n - i\kappa)^2 \equiv \tilde{n}^2, \tag{10}$$

such that the inhomogeneous vector curl-curl equation becomes [36]

$$\vec{\nabla} \times \left(\vec{\nabla} \times \vec{E}\right) = \zeta_0^2\tilde{n}^2\vec{E}. \tag{11}$$

Note that the magnetic field can be (re-)obtained through the original Maxwell's equations, i.e. through Faraday's law as [31, 34, 36]

$$\vec{H} = -\frac{i}{\omega\mu}\vec{\nabla} \times \vec{E}, \tag{12}$$

7

where $\vec{H}$ is the magnetic field.

This notation is convenient in optics considering $n = \lambda_0/\lambda$ is the refractive index and κ is the extinction coefficient of the material. As the name suggests, κ captures a similar phenomenon as the absorption coefficient α in Eq. (2), and they can be related through [36–38]

$$\kappa = \frac{\alpha c}{2\omega} = \frac{\alpha \lambda}{4\pi}. \tag{13}$$

The electric and magnetic fields are related to the local intensity through the Poynting vector

$$\vec{S} = \vec{E} \times \vec{H}^*, \tag{14}$$

where $\vec{H}^*$ denotes the complex conjugate of $\vec{H}$. The intensity then follows from the magnitude of the time averaged Poynting vector [35, 36, 39], i.e.

$$I = \langle \vec{S} \rangle = \left| \frac{1}{2} \mathfrak{R} \left\{ \vec{E} \times \vec{H}^* \right\} \right|. \tag{15}$$

In the limit case of a homogeneous (non-scattering) medium, Eq. (15) and Eq. (2) provide the same intensity field information. For heterogeneous media, Eq. (15) provides the near-field information required to describe the polymerization process.

2.2. Polymerization

The light energy flux propagating through the resin is a direct initiator for the polymerization reaction. In order to quantify polymerization, a degree of conversion is defined based on the current and initial monomer concentration [40] ($[M]$ and $[M]_0$, respectively) as

$$p = \frac{[M]_0 - [M]}{[M]_0}. \tag{16}$$

To relate the conversion to the intensity a rate type kinetic evolution equation will be used.

Cure kinetics. The resins that are generally used in vat photopolymerization of ceramics are acrylate-based [4], which implies kinetics of the free-radical (chain) polymerization type [41]. A reaction of this type consists of three sequential steps, thus called a chain reaction, i.e. initiation, propagation and termination.

8

The initiation step begins with the creation of free radicals by the initiator molecule. The rate of radical generation is driven by the amount of light absorbed [24, 42]. A generally used expression for this is written in terms of the rate of initiation R_i as

$$R_i = 2\psi I_a, \tag{17}$$

where ψ is the quantum yield for initiation and I_a the absorbed light intensity [41]. The primary or initiator radical reacts with a monomer to form the chain-initiation species.

During propagation the initiated chains grow into long chains. At some point the propagation reaction arrests and termination occurs. This phenomenon mainly originates from two reactive species, combining into a non-reactive polymer. As a result from the propagation reaction, the monomer concentration decreases as the conversion progresses, which forms the motivation for Eq. (16).

Formally, the monomer evolution can be specified as

$$-\frac{d[M]}{dt} = R_i + R_p, \tag{18}$$

where R_p is the rate of propagation. The rate of monomer disappearance, which is identical to the rate of polymerization, is thus equal to the rate of propagation. In order to derive an equation for the monomer evolution, the rate of propagation is written as

$$R_p = k_p[M\bullet][M] \tag{19}$$

where k_p is the rate constant for propagation and $[M\bullet]$ is the concentration of chain radicals. Subsequently, a steady-state assumption is made on the concentration of radicals [40–42], i.e.

$$R_i = R_t = 2k_t[M\bullet]^2, \tag{20}$$

with k_t the rate constant for termination. Eq. (20) provides a relation for $[M\bullet]$ as a function of R_i, which, together with Eq. (17), can be substituted in Eq. (19) to obtain

$$R_p = -\frac{d[M]}{dt} = k_p[M]\left(\frac{\psi I_a}{k_t}\right)^{1/2}. \tag{21}$$

Such a formulation allows to account for temperature dependent effects through the kinetic parameters, by expressing them as an Arrhenius-type relationship [41]. Accounting for e.g. oxygen as an inhibitor species can also be done [18]. Furthermore,

it is possible to account for photobleaching of the solution through a time-dependent (absorbed) intensity, which is caused by the depletion of the initiator [43–46]. Additionally, the polymerization may effect the refractive index of the polymer [47].

In the following, the cure kinetics are simplified further by lumping the different parameters in Eq. (21). The polymerization rate is then written as

$$R_p = -\frac{d[M]}{dt} = \mathcal{P}_M \sqrt{I}[M],$$

(22)

where $\mathcal{P}_M$ is the lumped polymerization constant, i.e. no time dependence is accounted for, and the absorbed intensity I_a is replaced by the actual intensity I. Note that the latter implies that the absorbed intensity I_a is assumed to be a constant fraction of the actual intensity I. Diffusional effects are not accounted for.

2.3. Thermodynamics

In a typical photo-polymeric suspension, heat generation is twofold. Firstly the photopolymerization reaction is exothermic, thus generating heat. Secondly, light absorption by the photoinitiator or its decomposition products, the dye, the monomer or polymer constitutes a thermal source. However, due to transparency for ultraviolet wavelengths, the absorption of most monomer and polymers is negligible in the considered regime.

The energy balance equation which incorporates these effects is adapted from [24] as

$$\rho c_p \frac{dT}{dt} = \nabla \cdot (k \nabla T) - \Delta H \, \frac{d[M]}{dt} + aI[C^*],$$

(23)

where the first two terms are the standard heat conduction terms, the third is the exothermic heat generation by the reaction and the last term accounts for heat generation by light absorption. The terms ρ, c_p and k in the first two terms correspond to the mass density, the heat capacity and the thermal conductivity, respectively. In the latter terms of Eq. (23), ΔH is the polymerization heat and a is the molar absorptivity. Under the assumption that the initiator is the only absorbing species, the latter $[C^*]$ can be replaced by $[In]$. It can also be noticed that the formulation in Eq. (23) does not contain direct

10

heat sources and mechanical dissipation is neglected. Thermal equilibrium is also required in the formulation of the constitutive behavior for the inclusions, although be it without source terms. Consequently, the description for the inclusions is limited to the first two terms in Eq. (23). Note that a perfect interface between the two materials is assumed, i.e. the presence of voids or other irregularities is not accounted for.

2.4. Mechanics

In this work the mechanical response is linear elastic and restricted to small deformations. The total strain tensor ε is decomposed according to

$$\varepsilon = \varepsilon_{\mathrm{e}} + \varepsilon_{\mathrm{ch}} + \varepsilon_{\mathrm{th}}, \tag{24}$$

into an elastic, chemical and thermal component, respectively. This is sufficient to illustrate the effect of the coupling between individual phenomena. Note that both matrix and inclusions undergo thermal strains, but $\varepsilon_{\mathrm{ch}}$ is limited to the resin. Explicitly accounting for the individual components' behavior through a full-field approach provides insights into e.g. the residual stress development.

Chemical shrinkage. An effect that occurs upon conversion of monomer molecules into long polymer chains is the contraction of inter-molecular spacing. Specifically, the distance corresponding to the van der Waals interaction is replaced by a reduced intra-molecular covalent bond [40, 48]. The amount of volumetric shrinkage $\frac{\Delta V}{V}$ can be estimated semi-analytically as a function of the conversion, through [49]

$$\frac{\Delta V}{V} = 22.5 p \frac{\sum_i \left(f_i \chi_i \right)}{M_{mi} \chi_i} \rho, \tag{25}$$

where f_i, χ_i and M_{mi} are the monomer functionality, mole fraction and molecular mass, respectively, p is the degree of conversion which follows from Eq. (16) and ρ is the initial density of the monomer mixture. The factor 22.5 is the experimentally derived volume change per mole of the reacting group [14, 49, 50], which is here assumed to be an acrylate. The linear shrinkage strain can then be written as

$$\varepsilon_{\mathrm{ch}} = \frac{1}{3} \frac{\Delta V}{V} I, \tag{26}$$

11

where isotropic shrinkage is assumed and, correspondingly, I is the unit tensor. In the following this is reformulated as

$$\boldsymbol{\varepsilon}_{\text{ch}} = p \boldsymbol{\varepsilon}_{\text{ch,max}} \boldsymbol{I}, \tag{27}$$

with $\boldsymbol{\varepsilon}_{\text{ch,max}}$ following from Eqs. (25) and (26) with $p = 1$. Whereas this assumes a linear and direct relationship between conversion and shrinkage, models where the shrinkage lags behind the conversion also exist [51], albeit that these models are often of a phenomenological nature. Note that the ceramic inclusions do not undergo a chemical transformation, i.e. the chemical shrinkage is restricted to the resin.

Thermal expansion. The thermal strains are formulated according to the classical isotropic form

$$\boldsymbol{\varepsilon}_{\text{th}} = \upsilon \left(T - T_{\text{ref}} \right) \boldsymbol{I}, \tag{28}$$

where υ is the thermal expansion coefficient of the material and T and T_{ref} the current and reference temperature, respectively. Thermal straining affects both the resin and the ceramic inclusions, each with its respective thermal expansion coefficient.

Solidification. The build-up of mechanical properties in the matrix material is referred to as solidification, i.e. the elongation and cross-linking of polymer chains upon (photo)polymerization introducing solid-like behavior. Generally, the point where the material transforms from a liquid into a solid is termed the gel-point. From this point onward a direct relation between the conversion level and the elastic [5, 52], viscous [53–55] or even plastic properties [56] exists.

Transient phenomena will be ignored here, i.e. the solidification only consists in a conversion dependent Young's modulus. The relation between conversion and elasticity is taken direct and linear from the gel-point p_{gel} onwards [54], where the stiffness up to the gel-point is assumed to be $e_0 E_{\text{pol}}$ with $e_0 \ll 1$. Mathematically this reads as

$$
\begin{aligned}
E(p) &= e_0 E_{\text{pol}} && \text{for } p < p_{\text{gel}} \\
E(p) &= \left(\frac{1 - e_0}{1 - p_{\text{gel}}} \left(p - p_{\text{gel}} \right) + e_0 \right) E_{\text{pol}} && \text{for } p \geq p_{\text{gel}}
\end{aligned}
\tag{29}
$$

where $E(p)$ is the conversion dependent Young's modulus of the monomer/polymer. The resin and inclusion's stress tensors σ are related to the elastic strain tensors ϵ through the classical isotropic Hooke's law. Other mechanistic properties, such as the coefficient of thermal expansion, are taken constant, i.e. independent of the conversion, for simplicity.

2.5. Coupling of physical phenomena

The complete coupling between all phenomena introduced in the previous Sections 2.1 to 2.4 is illustrated in Fig. 2. A key assumption in the formulation of the
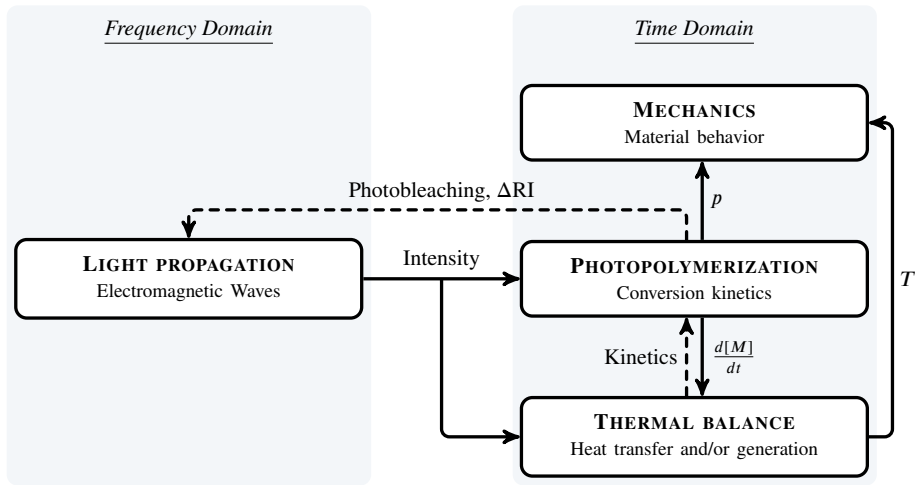

Figure 2: Overview of the proposed multiphysical coupling. Dashed lines have been mentioned in Section 2 but are currently not incorporated in the modeling framework.

multiphysical framework is the separation of time scales by separating between the frequency and time domain. This is justified by the large difference in time scales of the light propagation and the kinetics. For a vector scanning technique, as considered here, the transit time of a photon through a layer is in the order of a picosecond ($\sim 10^{-12}$ s), whereas the kinetic reaction duration is typically of the order of (several) microseconds ($\sim 10^{-6}$ s) [1, 5]. It is expected that the other physical phenomena are coupled to the reaction time.

From a numerical point of view, this implies that a steady-state response is obtained for the light propagation in the harmonic frequency domain, corresponding to the light

13

source conditions. Subsequently, Eq. (15) is used to extract the effective time average intensity field, which provides the required input for the time-domain simulation of the chemical conversion (and absorption heat) and the emanating phenomena indicated in Fig. 2.

2.6. Implementational aspects

Solving Maxwell's equations in a finite element framework imposes additional requirements on the discretization. In order to properly resolve the wavelike behavior, a minimal number of 10 elements is required over the wavelength [35], whereas the actual wavelength inside the different constituents is typically reduced by a refractive index > 1, according to $\lambda = \lambda_0/n$. This clearly poses a restriction on the feasibility of solving large structures, considering the wavelength of the applied UV light is only approximately 400 nm. Restricting the simulation to a finite domain requires special absorbing boundary conditions to prevent scattering from the bounding frame. This requirement is incorporated in the form of a so-called perfectly matched layer (PML) [57]. Furthermore, in order to prevent spurious solutions in inhomogeneous media, a special type of elements is used with degrees of freedom assigned to the edges instead of the nodes, referred to as edge elements. The requirement for these vector or Nédélec elements originates from the lack of enforcement of the Maxwell divergence condition by regular nodal elements, which has been described in detail in Refs. [31, 32, 58, 59]. The complete modeling framework as depicted in Fig. 2 is implemented in the finite element package Comsol 5.0 [60]. A fully-coupled approach is used, employing a direct solver. The backward Euler time stepping is automated through a variable-order variable-step-size backward differentiation algorithm [60]. No special measures were required to ensure stability.

3. Verification

Before investigating the different physical phenomena in the example problem considered in Section 4, the correctness of the numerical framework is assessed first. To do so, the different components of the modeling framework are compared to analytic solutions using identical parameter-sets in the following.

14

3.1. Intensity

An important component of the proposed model (cf. Fig. 2) is the electromagnetic wave description, particularly the near-field information predicted for the intensity field. It remains to be verified whether the numerical implementation of the Maxwell's equations correctly approximates the expected scattering. To this purpose, the predicted result for a single scattering particle is compared to the analytic near-field Mie theory implementation by Schäfer et al. [61]. An example result is shown in Fig. 3. Here the

(a) Computed normalized intensity profile

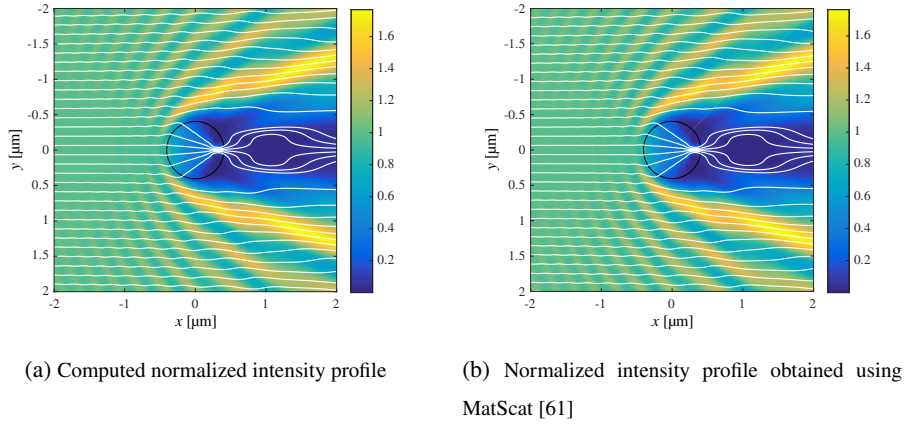(b) Normalized intensity profile obtained using MatScat [61]

Figure 3: Comparison of results for the field intensity obtained from the present framework and MatScat for a particle with $r = \lambda$, $\tilde{\epsilon}_r = 4 - 0.5i$. Intensity is normalized by the source intensity. Streamlines of the Poynting vector are depicted in white.

matrix material and the particle have a (complex) relative permittivity of $\tilde{\epsilon}_r = 1$ and $\tilde{\epsilon}_r = 4 - 0.5i$, respectively. In the current example, absorption by the polymer is neglected. The input source is a homogeneous plane wave propagating towards the right with a polarization in the direction perpendicular to the xy-plane, i.e. the out-of-plane z-direction. Note that in the case of a polymer matrix, this material would also absorb light, i.e. have a complex component in the permittivity, but the implemented Mie theory does not allow for this. The radius of the particle is equal to the wavelength $\lambda = 400$ nm. In order to visualize the results in Fig. 3a, the field data obtained with the implemented numerical framework was interpolated using natural neighbor interpolation.

The depicted intensity profile and power flow lines in Fig. 3 clearly reveal that the

15

wavelike behavior, e.g. not only refraction and attenuation but also diffraction, is cor-
rectly captured. The mean difference in the depicted field (also accounting for interpo-
lation errors) is only 1%. Fig. 3 also emphasizes the relevance of a wave description for
these length scales.

3.2. Conversion

The polymerization model is implemented through the Comsol PDE interface [60].
In order to verify this part of the implementation, a domain is polymerized by a constant
and homogeneous intensity field I_0. This allows for an analytical solution for $d[M]/dt$
derived from Eq. (22) as

$$\frac{d[M]}{dt} = -[M]_0 \mathcal{P}_M \sqrt{I_0}\, e^{-\mathcal{P}_M \sqrt{I_0}\, t}.$$
(30)

Due to the homogeneous intensity, the considered domain can be from one to three-
dimensional. Eq. (30) is then compared to the evolution of the numerically derived
$\mathcal{P}_M \sqrt{I_0}[M]$. Parameter values as specified in Tables 1 and 3, with $I_0 = I_{\max}$ are used.
Furthermore, because $d[M]/dt$ enters the thermal balance in Eq. (23), the numerical time
derivation is also included in the comparison. The solution for a two-dimensional do-
main of $1 \times 1\ \mu\mathrm{m}^2$ is shown in Fig. 4. Small deviations from the analytic result are
observed in Fig. 4, particularly where the slope is the highest, but overall the corre-
spondence is adequate.

3.3. Temperature

A similar approach compared to the previous conversion verification in Section 3.2
with a homogeneous illumination is also used in the thermal verification assuming ther-
mally insulated boundaries. The result of this comparison is shown in Fig. 5 for a ho-
mogeneous $1 \times 1\ \mu\mathrm{m}^2$ domain where the analytical (combined) prediction is derived
from Eq. (23) as

$$T = T_0 + \frac{1}{\rho c_p} \left(\underbrace{\Delta H \frac{d[M]}{dt}}_{\text{chemical}} + \underbrace{a I_0 [In]}_{\text{absorption}} \right) t.$$
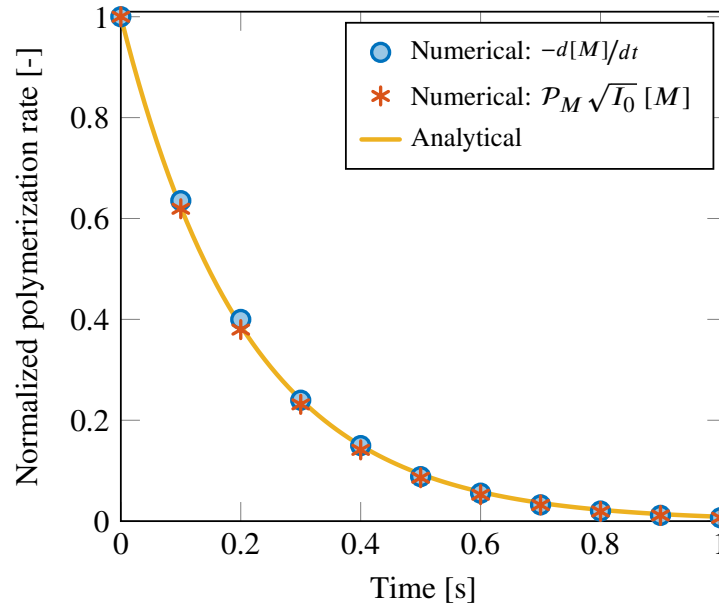(31)

16

Figure 4: Comparison of the numerical derived $d[M]/dt$ with the right hand side of Eq. (22) and the analytic form resulting from constant intensity illumination of I_0. Values are normalized by $\frac{d[M]}{dt}(t = 0)$ from Eq. (30).
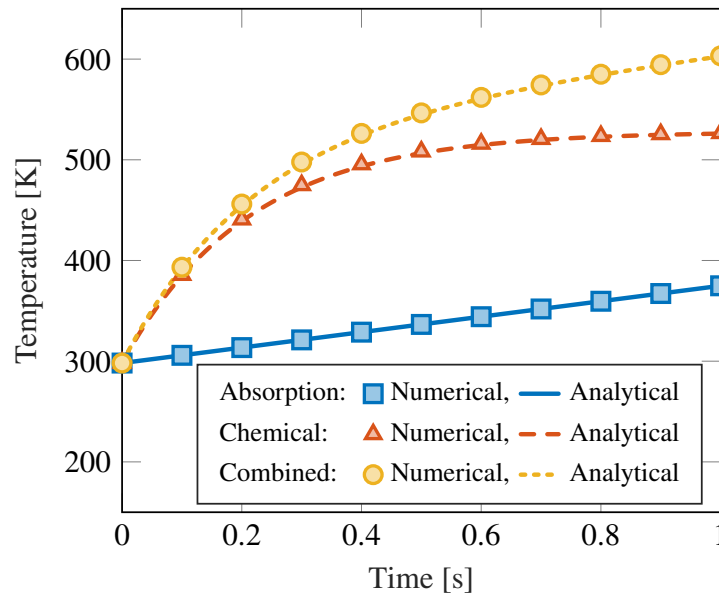

Figure 5: Comparison of the numerically obtained temperature increase with the analytical solution in terms of the absorption, exothermic and combined heat.

Parameter values are again adopted from Tables 1 and 3 with $I_0 = I_{max}$. For the

235 depicted absorption contribution to the temperature profile, the chemical component is set to zero and vice versa. The large temperature increase seen in Fig. 5 results from the material parameters and can also be seen in Ref. [24]. It is clear that the contribution of heat from absorption is less significant compared to the exothermic heat for the considered light intensity. Again, Fig. 5 shows adequate correspondence of the numerical

240 results compared to the analytic prediction.

3.4. Stress

Upon solidification, the polymer resin generally shrinks, as clarified in Section 2.4. At the same time, due to the exothermic nature of the reaction, thermal expansion occurs. As these strains, together with the conversion dependent mechanical properties, induce a stress build-up in the photopolymerization process, it is key to account for the combined effect correctly. This is illustrated in Fig. 6 for the same homogeneous 1×1 μm^2 domain. The square domain's lower left corner is fixed, while the bottom edge
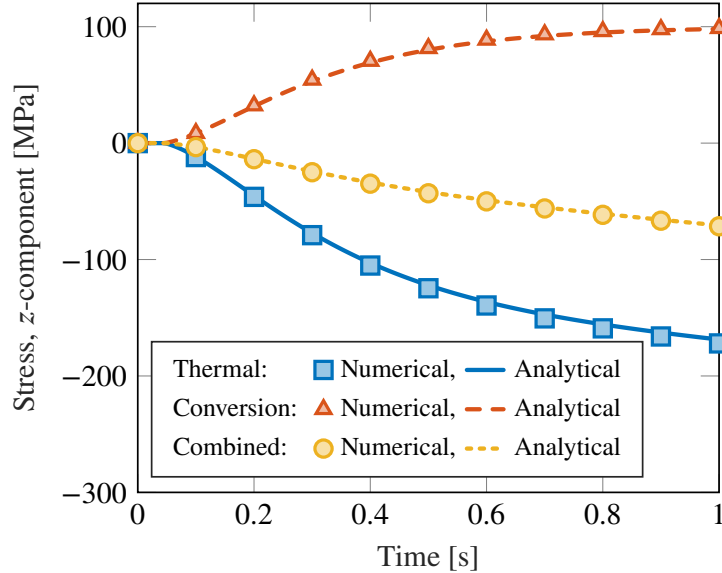

Figure 6: Comparison of the numerically obtained stress with the analytical response in the constrained (plane strain) z-direction, for the thermal, chemical and combined components. The difference is the propagated error from the polymerization and thermal prediction.

18

is only constrained in the vertical direction. The left, right and upper edge are unconstrained. Fig. 6 depicts the stresses predicted numerically in a constrained, i.e. plane strain z-direction and compares them to the analytical result. The analytical stress components in the constrained direction can be obtained as

$$\sigma_{z,\text{ch}} = \varepsilon_{\text{ch,max}} p E \tag{32}$$

and

$$\sigma_{z,\text{th}} = \upsilon \left(T - T_{\text{ref}} \right) E, \tag{33}$$

where $E = E(p)$ through Eq. (29) and $T = T(p)$ through Eq. (31). The initial zero slope of the lines depicted in Fig. 6 at $t = 0$ s illustrates the effect of the gel-point. Note that the numerical prediction uses the previously discussed addressed numerical values as input. The difference between the numerical and analytical value is therefore the error that propagated through the polymerization and thermal model, starting from the homogeneous intensity.

4. Application to an example problem

The goal of the example problem is to demonstrate the potential of the described approach and to illustrate the influence of the ceramic inclusions in the photopolymerization process. The necessary model input will be addressed in Section 4.2, after which Section 4.3 discusses the results.

4.1. Problem description

In order to illustrate the effect of the ceramic inclusions, three distinct geometries are considered, which are depicted in Figs. 7a to 7c: *(1)* an unfilled resin (Fig. 7a); *(2)* a slurry with an inclusion filling fraction ϕ of 0.4 distributed in a hexagonal grid (Fig. 7b); *(3)* a random distribution of particles with $\phi = 0.4$ (Fig. 7c). The size of the considered square domains is 11×11 μm^2, whereas the particles have a uniform diameter of 1 μm. The only difference between the different configurations is the distribution of the ceramic inclusions, i.e. the properties and boundary/initial conditions are identical. This

19

(a) Unfilled resin: A (b) Hexagonal grid: B (c) Random distribution: C
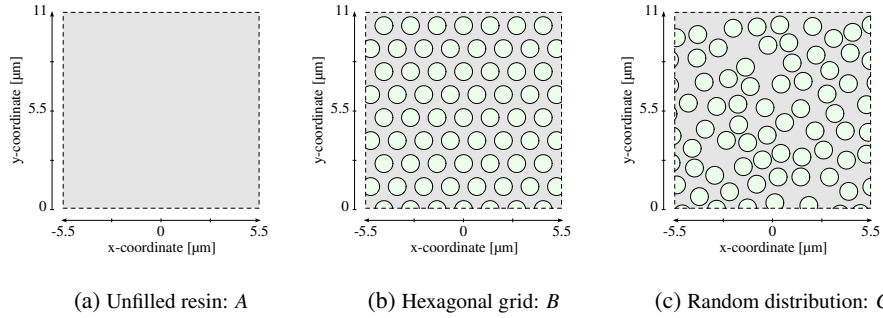
Figure 7: Example problem geometries with $\phi = 0$ in (a) and $\phi = 0.4$ in (b) and (c).

allows to study the relevance of the particulate inclusions and the randomness in their distribution. In the following, the unfilled resin, the matrix with particles positioned in a hexagonal grid and the arbitrarily distributed geometry will be referred to as case A, B and C, respectively.

Fig. 8 indicates the boundary conditions for the different physical models. The

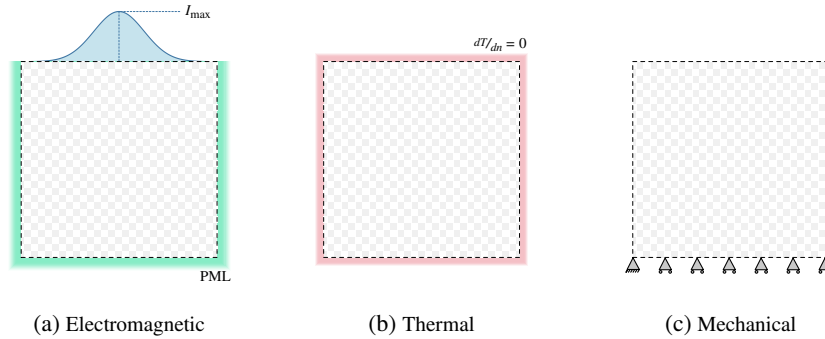(a) Electromagnetic   (b) Thermal   (c) Mechanical

Figure 8: Light (a), thermal (b) and mechanical (c) boundary conditions for the example problems introduced in Fig. 7. The polymerization reaction (not depicted) is limited to the resin and no flux occurs across the boundaries.

boundary conditions for the electromagnetic simulation are depicted in Fig. 8a. The top surface acts as a port for the incoming light intensity, which shows a Gaussian (laser) profile with a maximum intensity I_{max} at $x = 0$. The profile's spatial dependence is

formulated as

$$I_{\text{port}} = I_{\text{max}} e^{-x^2/w_0^2},$$

(34)

where w_0 is the beam half width where the intensity drops to $1/e^2$ of the value on the beam axis. The wave propagates in the negative y-direction with a polarization in the direction perpendicular to the xy-plane. Additionally, a Gaussian pulse is introduced, entailing an explicit time dependence, such that Eq. (34) can be extended to

$$I_{\text{port}} = I_{\text{max}} e^{-x^2/w_0^2} e^{-(t-t_{\text{max}})^2/2\tau^2}$$

(35)

where t_{max} is the time where the peak intensity occurs, and τ is a characteristic for the width temporal of the Gaussian "bell" shape. In order to simulate a finite domain and to prevent spurious reflections from the domain boundaries, absorbing boundary conditions are enforced at the bottom and left/right edges, in the form of a perfectly matched layer (PML) [35, 57]. Note a PML essentially extends the computational domain. Actual time steps taken by the backward differentiation time-stepping algorithm do not exceed 0.01 s, allowing to completely resolve the pulsed light excitation and the emanating physics.

The polymerization reaction, as introduced in Section 2.2, only actively influences the resin domain. No flux conditions are enforced on the outer boundaries and along the interfaces with the inclusions.

Fig. 8b illustrates the thermally insulated conditions assumed for the heat balance Eq. (23), i.e. $dT/dn = 0$. The result from these conditions is that the generated heat is internally contained and the thermal effect of the included particles is easily deduced.

Finally, the mechanical boundary conditions are illustrated in Fig. 8c. The left bottom point is constrained in all directions, whereas for the remainder of the bottom edge the vertical displacement is suppressed. The left, right and top edges are not constrained. A plane stress assumption is made in the two-dimensional representation. These particular choices prevent the buildup of macroscopic (average) stresses. Consequently, the buildup of microscopic stress around the rigid-like inclusions can be easily identified.

4.2. Model parameters

In order to illustrate the capabilities of the proposed model, a representative set of parameters is introduced. The material parameters are provided in Tables 1 and 2 for the resin and ceramic inclusions, respectively.

Table 1: Material properties for the resin.

Parameter	Value	Unit	Description	Source
n	1.5	[-]	Refractive index	[47, 62]
$[In]_0$	5	[mol/L]	Initial initiator concentration	
a_{In}	150	[L/(mol cm)]	Molar absorptivity initiator	[24]
$[M]_0$	8.2	[mol/L]	Initial monomer concentration	[24]
$\mathcal{P}_M$	0.15	[m^2/W]	Polymerization rate constant	[63]
c_p	1700	[J/(kg K)]	Heat capacity	[60]
ρ	1150	[kg/m^3]	Density	[60]
k	0.26	[W/(m K)]	Thermal conductivity	[60]
ΔH	$5.48 \cdot 10^4$	[J/mol]	Polymerization heat	[24]
E_{pol}	$2 \cdot 10^9$	[Pa]	Young's modulus at $p = 1$	[60]
e_0	$1 \cdot 10^{-3}$	[-]	Initial multiplication factor E_{pol}	
p_{gel}	0.2	[-]	Gel-point for conversion	[4]
ν	0.4	[-]	Poisson's ratio	[60]
$\epsilon_{\text{ch,max}}$	-0.05	[-]	Maximum shrinkage strain	[14]
υ	$280 \cdot 10^{-6}$	[1/K]	Coeff. of thermal expansion	[60]

The first section in Tables 1 and 2 provides the required material input with respect to the electromagnetic modeling. Alumina particles are chosen as they provide a relatively large contrast in refractive index compared to the resin, cf. 1.78 to 1.5. Whereas the refractive index of alumina is a well-established value [47], the value for the resin is only approximate considering the broad range in monomer refractive indices and its increase during polymerization [47, 62]. The ceramic inclusions are assumed to be transparent for UV-light [4]. Consequently, only the resin's extinction coefficient is nonzero, and obtained through Eq. (13) using $\alpha = \ln(10)a_{In}[In]$ (cf. Section 2.1). The

22

Table 2: Material properties for the alumina inclusions.

Parameter	Value	Unit	Description	Source
n	1.78	[-]	Refractive index	[47]
κ	0	[-]	Extinction coefficient	[4]
c_p	900	[J/(kg K)]	Heat capacity	[60]
ρ	3900	[kg/m^3]	Density	[60]
k	27	[W/(m K)]	Thermal conductivity	[60]
E	$300 \cdot 10^9$	[Pa]	Young's modulus	[60]
v	0.222	[-]	Poisson's ratio	[60]
υ	$8 \cdot 10^{-6}$	[1/K]	Coeff. of thermal expansion	[60]

(initial) initiator magnitude $[In]_0$ is increased with respect to Ref. [24] to enhance the effect of absorption in the considered domain. As a consequence the light extinction increases, but the path the light traverses remains the same.

For the polymerization prediction, the initial monomer concentration and the polymerization rate constant suffice. The initial monomer concentration is adopted from Ref. [24]. The magnitude of the polymerization rate constant is motivated by fitting of Eq. (22) to Fig. 6 from Ref. [63] whilst accounting for the intensity dependence.

Thermal properties such as heat capacity and thermal conductivity for both the alumina particles and the representative polymer (i.e. nylon was chosen in this case) follow from Ref. [60]. The polymerization heat is adopted from Ref. [24].

The Young's modulus (fully polymerized for the resin), the Poisson's ratio and thermal expansion values (assumed constant) follow from Ref. [60]. The initially small value of the modulus of the monomer is obtained by pre-multiplication of the fully polymerized Young's modulus with a value $e_0 = 1 \cdot 10^{-3}$. A representative linear chemical shrinkage strain active in the resin upon polymerization is chosen as 5% [14].

Initial and boundary conditions are specified in Table 3. Firstly, I_{max} and w_0 define the shape of the incoming light source at $t = t_{max}$, whereas secondly, τ dictates the time dependence of the input wave and, thirdly, λ is the wavelength. The initial temperature is set to 20 °C. Using the specified ultraviolet wavelength λ and the resin's and inclusion's

23

Table 3: Initial and boundary conditions.

Parameter	Value	Unit	Description
I_{max}	1000	[W/m^2]	Incident peak light intensity
w_0	2	[μm]	$^1/_{e^2}$ half-width of Gaussian beam
t_{max}	0.5	[s]	Time of peak intensity
τ	$^{0.4}/_3$	[s]	Pulse temporal standard deviation
λ	400	[nm]	Wavelength, vacuum
T_0	293	[K]	Initial temperature

refractive index n from Tables 1 and 2, the coupled multi-physical example problems incorporate $\mathcal{O}(10$ million) degrees of freedom.

4.3. Results and discussion

One of the key phenomena incorporated in the modeling framework is the propagation of the laser light through the matter. The intensity from the light is also the initiator for the onset of polymerization and consequently the generation of heat and the build-up of mechanical resistance and stresses. In this case, the predicted light intensity is a function of the electric field. The maximum electric wave amplitude which occurs at $t = t_{max} = 0.5$ s for the adopted polarization is depicted in Fig. 9. The result is
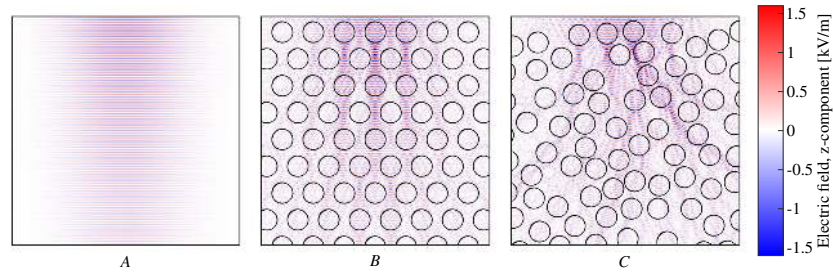

Figure 9: Electric field in the z-direction in the different geometries at $t = t_{max} = 0.5$ s.

shown at maximum illumination, because of the linearity in the Maxwell's equations, i.e. the wave magnitude throughout the domain scales linearly with the source magnitude. Fig. 9 illustrates the effect of the difference in refractive index on the wave

propagation through and around inclusions for cases *B* and *C*, introducing effects such as interference and diffraction. For case *A*, the result of the planar wave (which remains planar) shows a Gaussian distribution in magnitude over the width and the effect of extinction at increasing penetration depth. The same distribution can also be perceived in the intensity profile depicted in Fig. 10. Besides the intensity, which is normalized
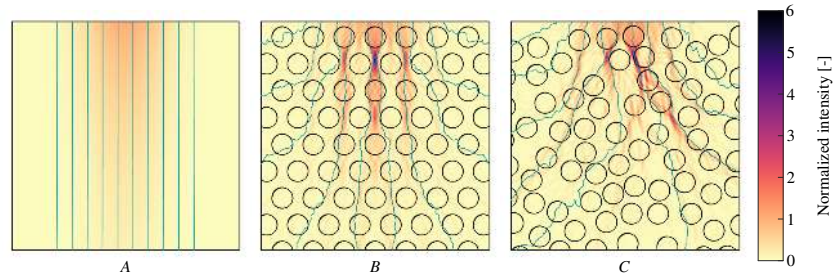

Figure 10: Intensity normalized with I_{max} and flow direction, i.e. direction of the Poynting vector, in the three geometries at $t = t_{\mathrm{max}} = 0.5$ s.

by the maximum intensity at the input port I_{max}, this figure also shows the streamlines of the power flow, i.e. the direction of the Poynting vector from Eq. (14). Here, the wavelike pattern has vanished but the interference and diffractional effects are more pronounced. Whereas case *A* illustrates the expected intensity profile from the Beer-Lambert law, cases *B* and *C* show a highly irregular light propagation. In addition to the inhomogeneous nature of the intensity, also large intensifications occur as a result from interference. From both the flow streamlines and the intensity concentrations, it is clear that the light still predominantly propagates towards the bottom of the specimen in case *B*. Nevertheless, a more severe scattering occurs in case *C*, where the inclusions are randomly distributed.

The latter trend also pushes through to the polymerization reaction as shown in Fig. 11. It shows the time dependent polymerization at $t = 0.2, 0.5$ and 1 s. These times are taken before, at and after the peak in illumination, respectively. Unlike case *A*, the cases with particles have a highly inhomogeneous conversion level after the pulsed illumination (at $t = 1$ s). This effect will reduce with a moving laser and/or by accounting for a more irregular geometry of the inclusions. Nonetheless, it clearly illustrates the
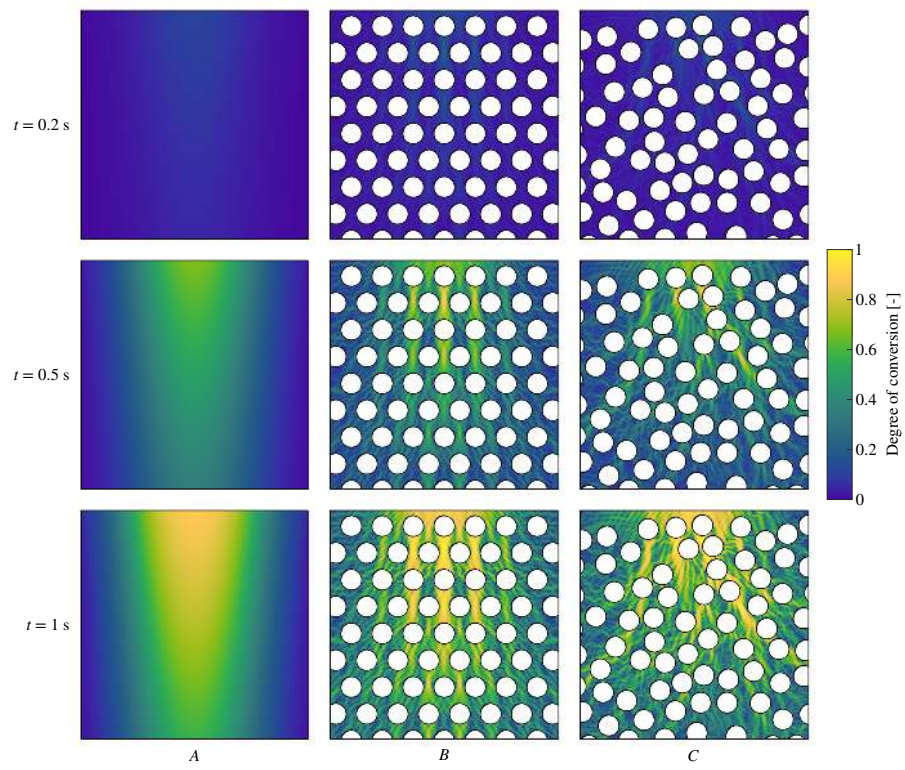
Figure 11: Degree of conversion p in the different geometries at $t = 0.2$, 0.5 and 1 s.

challenge to obtain a homogeneously polymerized product. This is an essential quality requirement, since the presence of residual monomer has been identified in relation to the formation of cracks during post-processing of the green part [64]. The average, minimum and maximum degree of conversion value obtained for the three different cases as a function of time are depicted in Fig. 12. As depicted, the average degree of
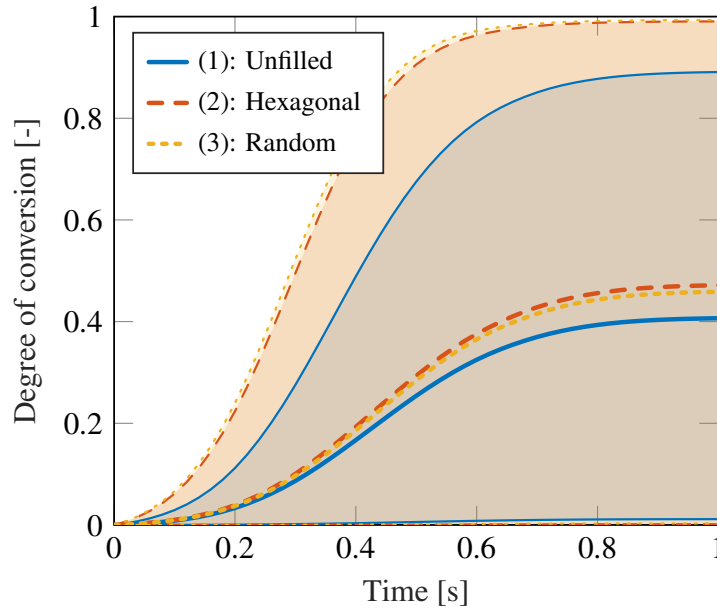

Figure 12: Evolution of the degree of conversion p for the different geometries with its mean value indicated by a thick line and the upper and lower bounds with a thin line.

conversion is higher for cases B and C with a value of $p_{\text{mean}} = 0.47$ and 0.45, respectively, compared to $p_{\text{mean}} = 0.41$ for case A. Note that this does not necessarily imply that one case is better than the other. The polymerization efficiency as reported here is dependent on the choice of domain dimensions, e.g. case A will be more efficient for a domain with a higher depth-to-width ratio. Fig. 12 does, however, further emphasize the pronounced inhomogeneity in the filled resin, considering the larger band between the minimum and the maximum value.

A direct result from the illumination and the polymerization is the accumulation of heat. Due to the small dimensions and the considered boundary conditions, the tem-

perature remains essentially homogeneous throughout the simulated domain, i.e. the temperature difference is only in the order of 10^{-2} K. At $t = 1$ s, the maximum temperature obtained in cases A, B and C is 388, 344 and 342 K, respectively. The most important conclusion is that the temperature increase is more significant in the unfilled resin. The explanation for this is twofold; firstly, the inclusions do not contribute to the reaction heat and, secondly, they act as a heat sink. The minor difference between case B and C results from the contrast in the average degree of conversion at $t = 1$ s, as shown in Fig. 12.

Finally, the polymerization results in residual stresses. In the solidification process a number of interesting effects accumulate. First, the conversion induces a chemical shrinkage in the resin following Eq. (27). Additionally, the polymerization reaction induced heat results in thermal expansion according to Eq. (28). The effect of the conversion is the build-up of stiffness, which is assumed linear after the gel-point as according to Eq. (29). Fig. 13 depicts the combined effect of these phenomena. The deformations, constituted by the simultaneous polymer chemical shrinkage and the composite's thermal expansion, illustrate the effect of the rigid-like ceramic inclusions. More severe warpage occurs in case A compared to cases B and C. Additionally, case A is the only geometry that effectively exhibits a volumetric expansion due to a higher temperature increase and effective thermal expansion coefficient. As larger deformations usually entail stress relaxation, the development of residual stresses is much smaller in case A compared to cases B and C. In order to highlight the stress concentrations, the color range is limited from $[0 - 60]$ MPa in Fig. 13, however, the peak stresses for case A, B and C at $t = 1$ s are 14, 76 and 128 MPa, respectively. The higher stress concentration in case C primarily originates from the more inhomogeneous particle distribution, compared to the hexagonal one. Juxtaposing Figs. 11 and 13 demonstrates the effect of introducing the gel-point in the solidification, i.e. it acts as a threshold for the development of stress. Overall, the stressed region in cases A and B is fairly narrow and deep, whereas case C illustrates a wider region of stress evolution. This is consistent with the more homogeneous contour of the deformed geometry.

The response of the example problems after cooling down to $T = T_0$ is shown in Fig. 14, using the same color bar as Fig. 13 to emphasize the difference. Elimination
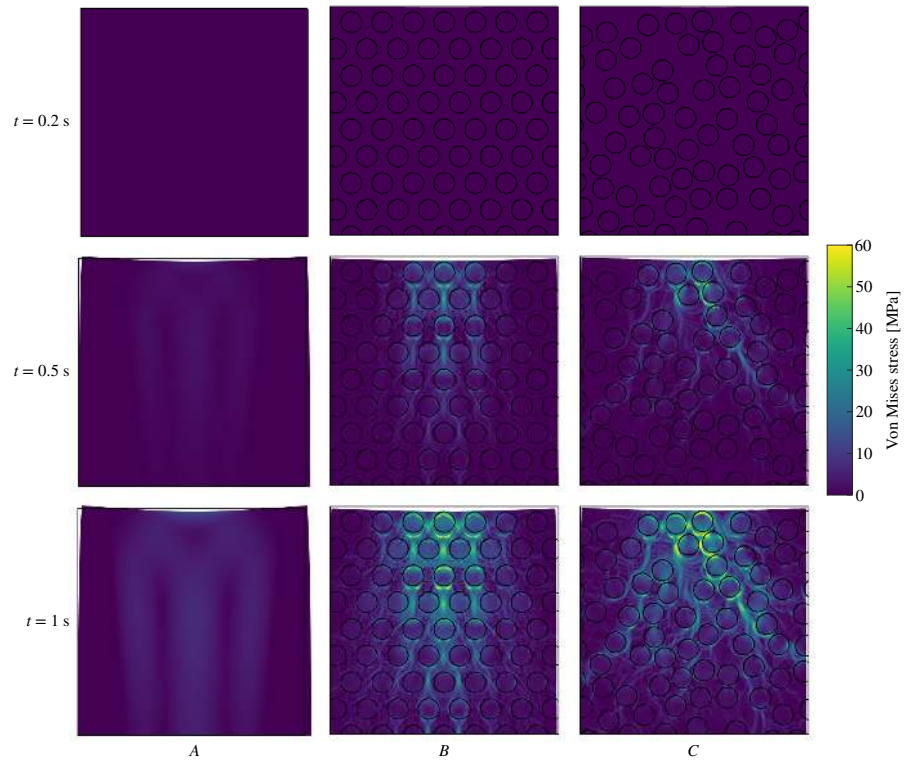
28

Figure 13: Von Mises stress and deformation in the different geometries at $t = 0.2$, 0.5 and 1 s. Solid lines depict the initial geometry. Deformations are scaled by a factor of 2. The peak stresses at $t = 1$ s are 14 MPa, 76 MPa and 128 MPa for cases A, B and C, respectively.
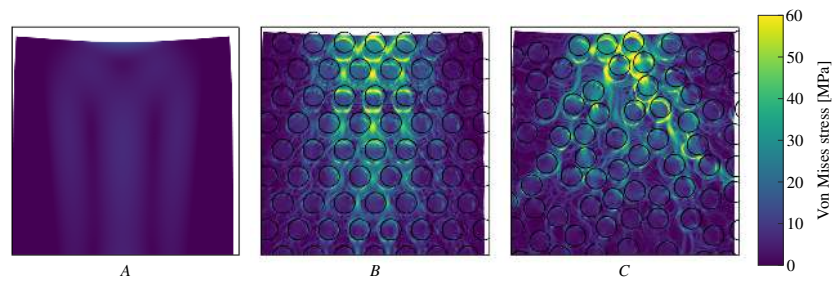

Figure 14: Von Mises stress and deformation in the different geometries after illumination and cooling down to $T = T_0$. Solid lines depict the initial geometry. Deformations are scaled by a factor of 2. The peak stresses are now 14 MPa, 106 MPa and 234 MPa for cases A, B and C, respectively. Color bar is adopted from Fig. 13.

of thermal expansion induces an increased stress for cases *B* and *C*, with peak stresses of 106 and 234 MPa, respectively. Due to the homogeneous thermal expansion, the peak stress remains 14 MPa in case *A*. With respect to the resulting deformations, the most notable difference occurs in case *A*, where the effective behavior is no longer a volumetric expansion. Due to the lower thermal expansion coefficient of the inclusions, the difference is less severe for the filled cases. Consequently, in case *A* the distortion reduces after cooling down, whereas for cases *B* and *C* it is less affected.

The presented example problem illustrates the significant effect of the addition of the inclusions on the propagation of light, the conversion reaction, the accumulation of heat and the solidification process. The expected curing pattern occurring in the homogeneous case *A* becomes severely distorted when randomly distributed inclusions are incorporated as in case *C*. In the present analysis the randomness is limited to the particle distribution only. The addition of more irregularities, such as particle size and shape, will have a supplementary effect on the dispersion of light through the matter. Additionally, the filling fraction of 40 % can be considered low with respect to ideal conditions for the post-processing of the green part. A higher filling fraction further increases the light dispersion. Cases *B* and *C* clearly highlight the relevance of the proposed approach to the model the coupled physical phenomena.

5. Conclusions

This paper proposes a coupled solution framework capturing distinct physical phenomena occurring in the vat photopolymerization process for ceramics. The numerical framework provides a direct coupling between a light source, via polymerization kinetics and temperature evolution, to the build-up of mechanical properties and residual stresses, resolved in space and time.

Accounting for the wavelike behavior of light illustrates the pronounced effects emerging when the size of microstructural features, i.e. the size of the particles, is of the same order as the wavelength, which is typical in AM for ceramics. The current polymerization model is relatively simple, only accounting for the dependence on monomer concentration and light intensity. Yet, it already highlights the impact of the resulting

30

inhomogeneous intensity on the solidification. The absorption of light combined with the exothermic polymerization causes the slurry to heat up. Due to the adopted thermally insulated boundary conditions, the final temperature is an upper bound, where the inclusions again have an influence. The accompanying thermal expansion is countered by a chemical shrinkage as polymerization progresses. This is illustrated in the proposed example problem, where a more homogeneous conversion results in a more homogeneous shrinkage. At the same time, the presence of rigid inclusions increases the magnitude of residual stresses. These trends remain after cooling down to the initial temperature, where the confined chemical shrinkage causes an increased residual stress state.

The model provides novel insights in the coupling between different physical phenomena in the photopolymerization process. The original and innovative contribution of this paper is a direct coupling between light scattering effects and photopolymerization related phenomena on a micro scale for a particulate medium. Whereas the framework can also be used for cure modeling in homogeneous resins, its real added value becomes clear in the presence of scattering particles with a size in the order of the wavelength. Although the considered model problems are two-dimensional, the developed modeling framework can also be devoted to three-dimensional cases. Future work will investigate to what extent the identified trends translate to three dimensions. It is expected that many of the model ingredients with respect to the distinct physical phenomena can be easily tailored to specific (slurry) systems of interest.

Acknowledgments

31

References

[1] I. Gibson, D. Rosen, B. Stucker, Additive Manufacturing Technologies, Springer New York, New York, NY, 2015. `doi:10.1007/978-1-4939-2113-3`. URL `http://link.springer.com/10.1007/978-1-4939-2113-3`

[2] J. R. G. Evans, Seventy ways to make ceramics, Journal of the European Ceramic Society 28 (7) (2008) 1421–1432. `doi:10.1016/j.jeurceramsoc.2007.12.015`. URL `http://www.sciencedirect.com/science/article/pii/S0955221907006103?via{%}3Dihub`

[3] A. Zocca, P. Colombo, C. M. Gomes, J. Günster, Additive Manufacturing of Ceramics: Issues, Potentialities, and Opportunities, Journal of the American Ceramic Society 98 (7) (2015) 1983–2001. `doi:10.1111/jace.13700`. URL `dx.doi.org/10.1111/jace.13700`

[4] J. W. Halloran, Ceramic Stereolithography: Additive Manufacturing for Ceramics by Photopolymerization, Annual Review of Materials Research 46 (2016) 10.1–10.22. `doi:10.1146/annurev-matsci-070115-031841`. URL `http://www.annualreviews.org/doi/10.1146/annurev-matsci-070115-031841`

[5] P. F. Jacobs, Rapid prototyping & manufacturing: Fundamentals of stereolithography, Society of Manufacturing Engineers in cooperation with the Computer and Automated Systems Association of SME, Dearborn, MI, 1992.

[6] V. Tomeckova, J. W. Halloran, Cure depth for photopolymerization of ceramic suspensions, Journal of the European Ceramic Society 30 (15) (2010) 3023–3033. `doi:10.1016/j.jeurceramsoc.2010.06.004`.

[7] S. P. Gentry, J. W. Halloran, Absorption effects in photopolymerized ceramic suspensions, Journal of the European Ceramic Society 33 (10) (2013) 1989–1994. `doi:10.1016/j.jeurceramsoc.2013.03.004`. URL `http://dx.doi.org/10.1016/j.jeurceramsoc.2013.03.004`

32

[8] S. P. Gentry, J. W. Halloran, Depth and width of cured lines in photopolymerizable ceramic suspensions, Journal of the European Ceramic Society 33 (10) (2013) 1981–1988. `doi:10.1016/j.jeurceramsoc.2013.02.033`.
URL `http://dx.doi.org/10.1016/j.jeurceramsoc.2013.02.033`

[9] S. P. Gentry, J. W. Halloran, Light scattering in absorbing ceramic suspensions: Effect on the width and depth of photopolymerized features, Journal of the European Ceramic Society 35 (6) (2015) 1895–1904. `doi:10.1016/j.jeurceramsoc.2014.12.006`.
URL `http://linkinghub.elsevier.com/retrieve/pii/S0955221914006633`

[10] Y. Huang, M. C. Leu, J. Mazumder, A. Donmez, Additive Manufacturing: Current State, Future Potential, Gaps and Needs, and Recommendations, Journal of Manufacturing Science and Engineering 137 (2015) 014001. `doi:10.1115/1.4028725`.
URL `http://manufacturingscience.asmedigitalcollection.asme.org/article.aspx?doi=10.1115/1.4028725`

[11] R. S. Chambers, T. R. Guess, T. Hinnerichs, A Phenomenological Finite Element Model of Stereolithography Processing, Tech. Rep. March, Sandia National Labs., Albuquerque (1996).
URL `https://www.osti.gov/scitech/servlets/purl/39693`

[12] Y.-M. Huang, S. Kuriyama, C. P. Jiang, Fundamental study and theoretical analysis in a constrained-surface stereolithography system, International Journal of Advanced Manufacturing Technology 24 (5-6) (2004) 361–369. `doi:10.1007/s00170-003-1627-9`.

[13] C.-P. Jiang, Y.-M. Huang, C.-H. Liu, Dynamic finite element analysis of photopolymerization in stereolithography, Rapid Prototyping Journal 12 (3) (2006) 173–180. `doi:10.1108/13552540610670753`.
URL `http://www.emeraldinsight.com/10.1108/13552540610670753`

[14] T. Wu, Theoretical modeling and experimental characterization of stress and crack development in parts manufactured through large area maskless photopolymerization, Phd thesis, Georgia Institute of Technology (2014).
URL `https://smartech.gatech.edu/bitstream/handle/1853/54274/WU-DISSERTATION-2014.pdf?sequence=1`

[15] N. Fang, C. Sun, X. Zhang, Diffusion-limited photopolymerization in scanning micro-stereolithography, Applied Physics A: Materials Science and Processing 79 (8) (2004) 1839–1842. `doi:10.1007/s00339-004-2938-x`.

[16] Y. Tang, C. Henderson, J. Muzzy, D. W. Rosen, Stereolithography cure modelling and simulation, International Journal of Materials and Product Technology 21 (4) (2004) 255. `doi:10.1504/IJMPT.2004.004941`.
URL `http://www.inderscience.com/link.php?id=4941`

[17] A. Boddapati, Modeling Cure Depth During Photopolymerization of Multifunctional Acrylates, Msc thesis, Georgia Institute of Technology (2010).
URL `https://smartech.gatech.edu/bitstream/handle/1853/33934/Boddapati{_}Aparna{_}201005{_}mast.pdf`

[18] A. S. Jariwala, F. Ding, A. Boddapati, V. Breedveld, M. A. Grover, C. L. Henderson, D. W. Rosen, Modeling effects of oxygen inhibition in mask-based stereolithography, Rapid Prototyping Journal 17 (3) (2011) 168–175. `doi:10.1108/13552541111124734`.

[19] H. W. Kang, J. H. Park, D. W. Cho, A pixel based solidification model for projection based stereolithography technology, Sensors and Actuators, A: Physical 178 (2012) 223–229. `doi:10.1016/j.sna.2012.01.016`.
URL `http://dx.doi.org/10.1016/j.sna.2012.01.016`

[20] W. Yan, W. Ge, Y. Qian, S. Lin, B. Zhou, W. K. Liu, F. Lin, G. J. Wagner, Multi-physics modeling of single/multiple-track defect mechanisms in electron beam selective melting, Acta Materialia 134 (2017) 324–333. `doi:10.1016/j.actamat.2017.05.061`.
URL `http://dx.doi.org/10.1016/j.actamat.2017.05.061`

[21] Z. Gan, H. Liu, S. Li, X. He, G. Yu, Modeling of thermal behavior and mass transport in multi-layer laser additive manufacturing of Ni-based alloy on cast iron, International Journal of Heat and Mass Transfer 111 (2017) 709–722. `doi:10.1016/j.ijheatmasstransfer.2017.04.055`.

URL `http://dx.doi.org/10.1016/j.ijheatmasstransfer.2017.04.055`

[22] A. Schmocker, A. Khoushabi, C. Schizas, P.-E. Bourban, D. P. Pioletti, C. Moser, Photopolymerizable hydrogels for implants: Monte-Carlo modeling and experimental in vitro validation., Journal of biomedical optics 19 (3) (2014) 35004. `doi:10.1117/1.JBO.19.3.035004`.

URL `http://www.ncbi.nlm.nih.gov/pubmed/24615642`

[23] D. F. Swinehart, The Beer-Lambert Law, Journal of Chemical Education 39 (7) (1962) 333. `doi:10.1021/ed039p333`.

URL `http://pubs.acs.org/doi/abs/10.1021/ed039p333`

[24] M. D. Goodner, C. N. Bowman, Development of a comprehensive free radical photopolymerization model incorporating heat and mass transfer effects in thick films, Chemical Engineering Science 57 (2002) 887–900. `doi:10.1016/S0009-2509(01)00287-1`.

[25] B. D. Fairbanks, M. P. Schwartz, C. N. Bowman, K. S. Anseth, Photoinitiated polymerization of PEG-diacrylate with lithium phenyl-2,4,6-trimethylbenzoylphosphinate: polymerization rate and cytocompatibility, Biomaterials 30 (35) (2009) 6702–6707. `arXiv:NIHMS150003`, `doi:10.1016/j.biomaterials.2009.08.055`.

URL `http://dx.doi.org/10.1016/j.biomaterials.2009.08.055`

[26] C. Leiner, W. Nemitz, S. Schweitzer, F. P. Wenzl, P. Hartmann, U. Hohenester, C. Sommer, Multiple interfacing between classical raytracing and wave-optical simulation approaches: a study on applicability and accuracy, Optics Express 22 (13) (2014) 16048–16060. `doi:10.1364/OE.22.016048`.

35

[27] M. L. Griffith, J. W. Halloran, Scattering of ultraviolet radiation in turbid suspensions, Journal of Applied Physics 81 (6) (1997) 2538–2546. `doi:10.1063/1.364311`.
URL `http://scitation.aip.org/content/aip/journal/jap/81/6/10.1063/1.364311`

[28] H. Horvath, Gustav Mie and the scattering and absorption of light by particles: Historic developments and basics, Journal of Quantitative Spectroscopy and Radiative Transfer 110 (11) (2009) 787–799. `doi:10.1016/j.jqsrt.2009.02.022`.

[29] E. S. Thiele, R. H. French, Light-Scattering Properties of Representative, Morphological Rutile Titania Particles Studied Using a Finite-Element Method, Journal of the American Ceramic Society 81 (3) (1998) 469–479. `doi:10.1111/j.1151-2916.1998.tb02364.x`.
URL `http://doi.wiley.com/10.1111/j.1151-2916.1998.tb02364.x`

[30] S. F. Liew, S. M. Popoff, A. P. Mosk, W. L. Vos, H. Cao, Transmission channels for light in absorbing random media: From diffusive to ballistic-like transport, Physical Review B - Condensed Matter and Materials Physics 89 (22) (2014) 1–10. `arXiv:1401.5805`, `doi:10.1103/PhysRevB.89.224202`.

[31] J.-M. Jin, The Finite Element Method in Electromagnetics, 3rd Edition, John Wiley & Sons, Inc., Hoboken, New Jersey, 2014.
URL `http://eu.wiley.com/WileyCDA/WileyTitle/productCd-1118571363.html`

[32] P. Monk, Finite Element Methods for Maxwell's Equations, Oxford University Press, Newark, NJ, 2003. `doi:10.1093/acprof:oso/9780198508885.001.0001`.

[33] T. Scharf, Polarized Light in Liquid Crystals and Polymers, John Wiley & Sons, Inc., Hoboken, NJ, USA, 2006. `doi:10.1002/047007437X`.
URL `http://doi.wiley.com/10.1002/047007437X`

36

[34] L. Demkowicz, Computing with hp-adaptive finite elements: Volume 1 - One and Two Dimensional Elliptic and Maxwell Problems, Chapman and Hall/CRC, 2006.

[35] Comsol Multiphysics RF Module User 's Guide, Tech. rep., Comsol Multiphysics (2014).
URL www.comsol.com

[36] J. D. Joannopoulos, S. G. Johnson, J. N. Winn, R. D. Meade, Photonic crystals: molding the flow of light, 2nd Edition, Princeton University Press, 2008.
URL http://ab-initio.mit.edu/book/

[37] S. G. Jennings, R. G. Pinnick, J. B. Gillespie, Relation between absorption coefficient and imaginary index of atmospheric aerosol constituents., Applied Optics 18 (9) (1979) 1368–1371. doi:10.1364/AO.18.001368.

[38] E. Hecht, Optics, 4th Edition, Pearson, San Francisco, CA, 2002.

[39] A. Navid, L. Pilon, Effect of polarization and morphology on the optical properties of absorbing nanoporous thin films, Thin Solid Films 516 (12) (2008) 4159–4167. doi:10.1016/j.tsf.2007.10.117.

[40] D. C. Watts, Reaction kinetics and mechanics in photo-polymerised networks, Dental Materials 21 (2005) 27–35. doi:10.1016/j.dental.2004.10.003.

[41] G. Odian, Principles of Polymerization, John Wiley & Sons, Inc., Hoboken, NJ, USA, 2004. doi:10.1002/047147875X.
URL http://doi.wiley.com/10.1002/047147875X

[42] E. Andrzejewska, Photopolymerization kinetics of multifunctional monomers, Progress in Polymer Science (Oxford) 26 (4) (2001) 605–665. doi:10.1016/S0079-6700(01)00004-1.

[43] V. V. Ivanov, C. Decker, Kinetic study of photoinitiated frontal polymerization, Polymer International 50 (1) (2001) 113–118. doi:10.1002/1097-0126(200101)50:1<113::aid-pi594>3.0.co;2-x.

37

URL `http://dx.doi.org/10.1002/1097-0126(200101)50:1{%}3C113::`
`AID-PI594{%}3E3.0.CO;2-X`

[44] G. Terrones, A. J. Pearlstein, Effects of optical attenuation and consumption of a photobleaching initiator on local initiation rates in photopolymerizations, Macromolecules 34 (10) (2001) 3195–3204. `doi:10.1021/ma001235y`.

[45] G. A. Miller, L. Gou, V. Narayanan, A. B. Scranton, Modeling of photobleaching for the photoinitiation of thick polymerization systems, Journal of Polymer Science, Part A: Polymer Chemistry 40 (6) (2002) 793–808. `doi:10.1002/pola.10162`.

[46] S. J. Oh, S. C. Lee, S. Y. Park, Photopolymerization and photobleaching of n-butyl acrylate/fumed silica composites monitored by real time FTIR-ATR spectroscopy, Vibrational Spectroscopy 42 (2) (2006) 273–277. `doi:10.1016/j.vibspec.2006.05.028`.

[47] F. Aloui, L. Lecamp, P. Lebaudy, F. Burel, Relationships between refractive index change and light scattering during photopolymerization of acrylic composite formulations, Journal of the European Ceramic Society 36 (2016) 1805–1809. `doi:10.1016/j.jeurceramsoc.2016.01.033`.
URL `http://dx.doi.org/10.1016/j.jeurceramsoc.2016.01.033`

[48] M. Patel, M. Braden, K. Davy, Polymerization shrinkage of methacrylate esters, Biomaterials 8 (1) (1987) 53–56. `doi:10.1016/0142-9612(87)90030-5`.
URL `http://linkinghub.elsevier.com/retrieve/pii/0142961287900305`

[49] N. Silikas, A. Al-Kheraif, D. C. Watts, Influence of P/L ratio and peroxide/amine concentrations on shrinkage-strain kinetics during setting of PMMA/MMA biomaterial formulations, Biomaterials 26 (2) (2005) 197–204. `doi:10.1016/j.biomaterials.2004.02.028`.

[50] S. Loshaek, T. G. Fox, Cross-linked Polymers. I. Factors Influencing the Efficiency of Cross-linking in Copolymers of Methyl Methacrylate and Glycol Dimethacry-

lates 1, Journal of the American Chemical Society 75 (14) (1953) 3544–3550.
doi:10.1021/ja01110a068.
URL http://pubs.acs.org/doi/abs/10.1021/ja01110a068

[51] L. Flach, R. P. Chartoff, A Simple Polymer Shrinkage Model Applied to Stereolithography, in: Solid Freeform Fabrication Symposium, 1994, pp. 225–233.
URL   https://sffsymposium.engr.utexas.edu/Manuscripts/1994/
1994-23-Flach.pdf

[52] Y.-M. Huang, C.-P. Jiang, Curl distortion analysis during photopolymerisation of stereolithography using dynamic finite element method, The International Journal of Advanced Manufacturing Technology 21 (8) (2003) 586–595. doi:10.1007/s00170-002-1317-z.

[53] M. H. H. Meuwissen, H. A. De Boer, H. L. A. H. Steijvers, P. J. G. Schreurs, M. G. D. Geers, Residual stresses in microelectronics induced by thermoset packaging materials during cure, Microelectronics Reliability 44 (12) (2004) 1985–1994. doi:10.1016/j.microrel.2004.05.001.

[54] C. Koplin, R. Jaeger, P. Hahn, A material model for internal stress of dental composites caused by the curing process, Dental Materials 25 (3) (2009) 331–338. doi:10.1016/j.dental.2008.08.007.

[55] M. Hossain, P. Steinmann, Degree of cure-dependent modelling for polymer curing processes at small-strain. Part I: consistent reformulation, Computational Mechanics 53 (4) (2013) 777–787. doi:10.1007/s00466-013-0929-5.
URL http://link.springer.com/10.1007/s00466-013-0929-5

[56] C. Liebl, M. Johlitz, B. Yagimli, A. Lion, Simulation of curing-induced viscoplastic deformation: A new approach considering chemo-thermomechanical coupling, Archive of Applied Mechanics 82 (8) (2012) 1133–1144. doi:10.1007/s00419-012-0639-z.

[57] J.-P. Berenger, A perfectly matched layer for the absorption of electromagnetic waves, Journal of Computational Physics 114 (2) (1994) 185–200.

39

doi:10.1006/jcph.1994.1159.

675   URL   http://www.sciencedirect.com/science/article/pii/
S0021999184711594

[58] J. C. Nedelec, Mixed finite elements in R3, Numerische Mathematik 35 (3) (1980)
315–341. doi:10.1007/BF01396415.

[59] J. Pomplun, S. Burger, L. Zschiedrich, F. Schmidt, Adaptive finite element method
680   for simulation of optical nano structures, Physica Status Solidi (B) 244 (10) (2007)
3419–3434. arXiv:0711.2149, doi:10.1002/pssb.200743192.
URL http://doi.wiley.com/10.1002/pssb.200743192

[60] Comsol Multiphysics Reference Manual, 2014.
URL www.comsol.com

685 [61] J. Schäfer, S. C. Lee, A. Kienle, Calculation of the near fields for the scatter-
ing of electromagnetic waves by multiple infinite cylinders at perpendicular in-
cidence, Journal of Quantitative Spectroscopy and Radiative Transfer 113 (16)
(2012) 2113–2123. doi:10.1016/j.jqsrt.2012.05.019.

[62] E. Johansson, O. Lidström, J. Johansson, O. Lyckfeldt, E. Adolfsson, Influence of
690   Resin Composition on the Defect Formation in Alumina Manufactured by Stere-
olithography, Materials 10 (138) (2017) 11. doi:10.3390/ma10020138.
URL http://www.mdpi.com/1996-1944/10/2/138

[63] M. D. Goodner, C. N. Bowman, Modeling primary radical termination and
its effects on autoacceleration in photopolymerization kinetics, Macromolecules
695   32 (20) (1999) 6552–6559. doi:10.1021/ma9901947.

[64] C. J. Bae, J. W. Halloran, Influence of residual monomer on cracking in ceramics
fabricated by stereolithography, International Journal of Applied Ceramic Tech-
nology 8 (6) (2011) 1289–1295. doi:10.1111/j.1744-7402.2010.02578.x.